

A multilens measurement platform for high-throughput adhesion measurements*

Aaron M Forster¹, Wenhua Zhang¹, Alfred J Crosby²
and Christopher M Stafford¹

¹ Polymers Division, National Institute of Standards and Technology, Gaithersburg, MD 20899-8542, USA

² Department of Polymer Science and Engineering, University of Massachusetts, Amherst, MA 01003, USA

E-mail: aaron.forster@nist.gov

Received 4 May 2004, in final form 21 September 2004

Published 16 December 2004

Online at stacks.iop.org/MST/16/81

Abstract

Current high-throughput methodologies for measuring interfacial adhesion typically rely on serial or sequential testing of discrete or continuous libraries. We have developed a measurement platform that employs an array of micro-lenses to simultaneously measure adhesion at multiple points on a planar specimen library. This technique relies on the accurate measurement of the overall lens array displacement, rather than load and individual lens contact areas to quantify the work of adhesion using the Johnson, Kendall and Roberts (JKR) model. We demonstrate the ability of this technique to measure the work of adhesion (loading) and energy release rate (unloading) for a polydimethylsiloxane lens array against glass, and we compare our work of adhesion measurements to the traditional single-lens geometry. We find the work of adhesion measured with the multilens array is $18.9 \text{ mJ m}^{-2} \pm 9.4 \text{ mJ m}^{-2}$ compared to $20 \text{ mJ m}^{-2} \pm 5 \text{ mJ m}^{-2}$ for a single-lens experiment. Also, the micro-lens array deviates from the JKR model when the lens array displacement is comparable to lens height.

Keywords: combinatorial, high-throughput, JKR, adhesion, axisymmetric adhesion tests, multilens, polydimethylsiloxane, finite size effects

(Some figures in this article are in colour only in the electronic version)

1. Introduction

Combinatorial and high-throughput (C&HT) experimental design has been advanced by the pharmaceutical and catalysis industries to facilitate discovery of novel drugs and catalysts with the goal of accelerating the time-to-market for these new materials. Due to their ability to rapidly investigate a large multi-parameter space, there has been a growing effort to extend C&HT methods into many aspects of material science, including material property screening and materials discovery. This concept has been advocated by both industry [1–3] and academia [4, 5] and has resulted in an extension of C&HT

into areas such as coatings [1, 3, 4, 6, 7], tissue scaffolds [8, 9] and mechanical property measurements [10, 11].

The National Institute of Standards and Technology Combinatorial Methods Center (NCCMC) has focused on both fabricating gradient libraries and measurement methods capable of characterizing gradient library properties. In material science, a prevalent approach to combinatorial library design is to incorporate continuous material property gradients across a specimen. Gradients provide convenient access to a large parameter space, tunable by the range and slope of property change along the sample. Methodologies have been developed for creating gradients in surface energy [12], film thickness and morphology [13–15], temperature [16] and composition [17]. While gradient libraries provide the means to quickly create a multivariate parameter space, new toolsets

* Official contribution of the National Institute of Standards and Technology; not subject to copyright in the United States.

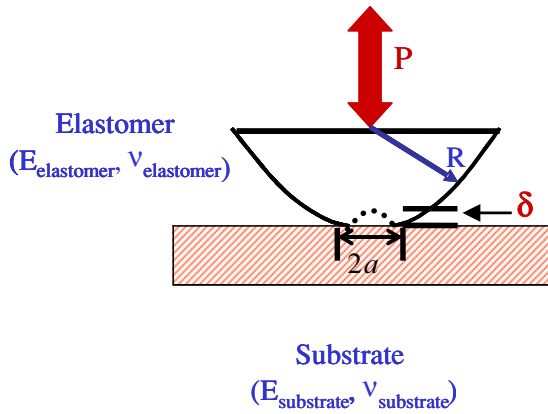


Figure 1. The axisymmetric adhesion test geometry. During testing the contact radius (a), load (P) and displacement (δ) are measured.

are continually required to measure material properties along these gradients. In this paper we describe a high-throughput axisymmetric adhesion test based on the contact mechanics theory first developed by Johnson, Kendall and Roberts [18]. We seek to define the bounds by which this adhesion test may be used to quantify the adhesion between two surfaces.

The JKR theory describes the contact area when two elastic hemispheres are brought together under load as a function of material properties and adhesion between the materials. This test is usually conducted by compressing and decompressing two hemispheres against each other and measuring load, contact area and displacement to provide a single adhesion measurement. Experimentally, the test geometry may also be a sphere against a flat substrate. This method may be applied in a serial manner for C&HT studies; however a serial approach results in a large amount of experimental time to completely characterize a combinatorial library. Another solution is to conduct parallel adhesion tests. In this manner, one loading and unloading cycle produces several adhesion tests and in a greater testing density than is possible with the traditional single-lens techniques. This is the motivation for the development of a multilens-contact adhesion test (MCAT) platform [16, 19, 20]. The MCAT technique, as will be shown, utilizes an array of hemispherical lenses to conduct multiple axisymmetric adhesion tests during one loading/unloading cycle.

2. Introduction to the JKR theory

The JKR theory is a modification of the Hertz equations of contact that takes into account the adhesive forces within the contact zone of two materials. The governing equations for this theory have been derived by several authors throughout the literature [21–23]. We provide a brief overview in this paper to accommodate a better understanding of the experimental analysis presented later. The equations may be derived by considering an elastic hemisphere brought into contact with a planar substrate under load (see figure 1). In this geometry, the elastic hemisphere is defined by its modulus (E), Poisson's ratio (ν) and radius of curvature (R). The equilibrium contact area, A , between the hemisphere and the planar substrate may

be described by considering an energy balance [24] over the system.

The system energy is the sum of the elastic energy stored within the deformed hemisphere, U_E , the potential energy of the load, U_P , and the interfacial energy, U_S . The derivative of total free energy must be a minimum at contact equilibrium, and we may take the derivative of the total free energy in the system to elicit two important terms: the change in potential energy of the system and the interfacial energy. The change in potential energy of the system is given by the potential energy of the load and the elastic energy stored within the hemisphere as a result of deformation as shown in equation (1)

$$\left. \frac{\partial U_E}{\partial A} \right|_P + \left. \frac{\partial U_P}{\partial A} \right|_P \quad (1)$$

where the first term is the elastic energy within the hemisphere, and the second term is the potential energy of the load. The interfacial energy is defined by

$$dU_S = -(\gamma_L + \gamma_S - \gamma_{LS}) dA = -W dA \quad (2)$$

where γ_L is the surface energy of the lens, γ_S is the surface energy of the substrate, γ_{LS} is the interfacial energy between the lens and substrate, and W is the thermodynamic work of adhesion. The energy required to increase surface area during the loading curve of an axisymmetric adhesion test is bounded by the thermodynamic work of adhesion (W), also known as Dupre's energy of adhesion, which is the energy required to reversibly separate two joined surfaces into two free surfaces [18, 24]. For adhesion testing we are often interested in the additional energy required to drive the separation between the two surfaces. Therefore, we now focus on the energy release rate. The energy release rate (\mathcal{G}) is defined using equation (1) and represents the amount of energy required to change contact area a unit amount. The solution for the energy release rate from equation (1), in the limit of small contact area, is given by [23]

$$\mathcal{G} = \frac{(P' - P)^2}{8\pi E^* a^3} \quad (3)$$

where $P' = 4E^* a^3 / 3R$ is the Hertz prediction of load, E^* is the system modulus, R is the radius of curvature of the lens and a is the contact radius. Equation (3) shows that the energy available for changing the contact radius is given by the difference between Hertz predictions (no adhesion) and the adhesive case. Equation (3) is valuable because it can be used to quantify velocity dependent adhesion processes. The system modulus, E^* , combines the contribution of both materials to the compliance of the system.

$$\frac{1}{E^*} = \frac{(1 - \nu_L^2)}{E_L} + \frac{(1 - \nu_S^2)}{E_S} \quad (4)$$

In equation (4), E_L and ν_L are the tensile modulus and Poisson's ratio for the lens; E_S and ν_S are the tensile modulus and Poisson's ratio for the substrate, respectively. For a rigid planar substrate and an elastic hemispherical lens the compliance results from the deformation of the lens. Therefore, the system modulus is dominated by the lens modulus and the substrate term in equation (4) is assumed to be zero. If the moduli of the lens material are known prior to the experiment, the system modulus may be calculated directly from equation (4).

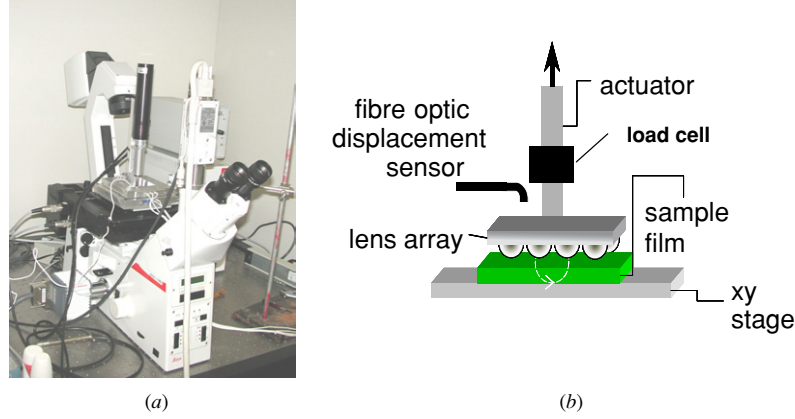


Figure 2. (a) Picture of complete MCAT instrument showing the actuator and tip/tilt stage attached to the inverted microscope. (b) Schematic of the MCAT axisymmetric adhesion test geometry. The lens array is attached to the nano-positioner actuator. Load is measured via a load cell and displacement is measured with a fibre optic displacement sensor (Philtec). The sample film is held fixed to the microscope x - y stage and the contact area is viewed through the film.

If the modulus of the lens material is not known, then equation (5) is often used to determine the system modulus by fitting experimental load, displacement and contact area data.

$$\delta_{\text{JKR}} = \frac{a^2}{R} + \frac{P}{2E^*a}. \quad (5)$$

Equation (5) is important because it provides a second method, independent of adhesion energy, to experimentally determine the system modulus.

One potential challenge of the current multilens technique is the inability to measure load on each lens of the array in conjunction with individual lens contact areas. In this case, equations (3) and (5) cannot be used to calculate \mathcal{G} without the load measurement. This challenge may be overcome by the use of the overall lens array displacement rather than the load and requires one to rearrange the energy release rate in terms of displacement rather than load, as was shown by several authors [22–24]. The system compliance, C , may be substituted into equation (3) to give the energy release rate, \mathcal{G} , as a function of displacement, δ .

$$C = \frac{2}{E^*a} = \frac{d\delta}{dP} = \frac{\delta' - \delta}{P' - P} \quad (6)$$

$$\mathcal{G} = \frac{E^*(\delta' - \delta)^2}{2\pi a} \quad (7)$$

where δ' is the Hertzian displacement given by a^2/R . Equation (7) may be rearranged to solve for δ to give the displacement-dependent form of the JKR equation.

$$\delta = \delta_0 + \delta' - \sqrt{\frac{2\pi a \mathcal{G}}{E^*}}. \quad (8)$$

In equation (8), δ_0 is the displacement at initial contact between the lens and substrate. From equation (8), we see that the displacement predicted for the adhesive case is always less than predicted by the Hertzian displacement. The initial contact between the lens and substrate is not directly measured in an experiment. Images of the contact between the hemisphere and substrate are taken during an experiment, but the initial contact often occurs slightly before the first image of contact. Uncertainty in the displacement at initial contact will also lead

to uncertainty in the measured \mathcal{G} . Therefore, δ_0 and \mathcal{G} are used as parameters to fit equation (8) to experimentally measured contact areas and the overall lens array displacement.

The displacement-based measurements should permit the determination of the work of adhesion at each lens of the multilens array for elastic contact using equation (8). However, Deruelle *et al* [22] have shown that displacement-based adhesion experiments deviate from the JKR theory more than corresponding load measurements due to the confinement of the lens. Since the lenses within the multilens array are much smaller than those used for single-lens JKR tests, we expect finite size effects will affect our ability to model the experimental data using the JKR equation. Our analysis will concentrate on whether the multilens system is affected by finite size effects and whether the \mathcal{G} measured with multilens experiments is comparable to single-lens experiments.

3. Multilens combinatorial adhesion test

3.1. MCAT apparatus

The multilens adhesion test apparatus is shown in figure 2 [19, 20]. The system consists of an inverted microscope (Leica DMIRE2) equipped with a programmable x - y stage and a CCD camera (Hamamatsu Photonics). Typically, a combinatorial gradient library is prepared on a transparent substrate (e.g., glass slide) and mounted onto the microscope translation stage for testing. The lens array is mounted onto an IW-812 piezoelectric nanopositioner (Burleigh Instruments) and positioned above the field of view (FOV) of the microscope objective. A load sensor (Sensotec) is attached in-line between the lens array and actuator shaft to monitor the overall system load. Displacement is measured by two fibre optic displacement sensors (Philtec) mounted above the translation stage holding the lens array. The displacement sensors measure the overall movement of the lenses and supporting substrate. It is possible that during the loading cycle, the lens substrate will compress in series with the lenses and the measured displacement is not the true displacement of each lens. The work of adhesion determined using the JKR theory will be sensitive to any uncertainty in the

displacement measurement. At this time, we cannot measure lens compression independent of substrate compression and, therefore, cannot address the influence of substrate compression on the work of adhesion measured with multilens arrays.

The actuator and lens array are mounted onto a second x - y translation stage that has two axis tip/tilt capabilities. The tip/tilt configuration permits micron resolution of the lens array alignment to bring the lenses parallel to the opposing planar substrate. The second x - y translation stage allows the user to raster the microscope objective to different areas of the lens array during adhesion testing and record contact area information from lenses outside the objective's initial FOV. This affords much more control over the lens array position for conducting multiple adhesion experiments.

LabView (National Instruments) software was used to build interfaces directly between the computer, image software and instruments. The LabView program directly controls the actuator and data acquisition, while indirectly coordinating image collection and microscope stage movement through Image Pro (Media Cybernetics) software.

3.2. Lens arrays and materials

Currently, we employ two different multilens array geometries for adhesion tests. The first array is a 1 cm^2 array containing 1600 lenses. Each lens in this array has a diameter of $250\ \mu\text{m}$ and a height of $22\ \mu\text{m}$ with a radius of curvature of $366\ \mu\text{m}$ (MEMS Optical Inc.). The lenses are configured in a square grid with a periodicity of $260\ \mu\text{m}$. The second array is also a square grid that is 3.25 cm^2 and contains 324 lenses. Each lens is $900\ \mu\text{m}$ in diameter and $300\ \mu\text{m}$ in height with a periodicity of $1000\ \mu\text{m}$ and a radius of curvature of $500\ \mu\text{m}$ (MicroFab Technologies). This work will focus on testing only the 1600 lens array against a model glass substrate.

3.3. Image analysis

One challenge with multilens adhesion tests lies in handling the volume of data generated during the adhesion test. At the end of an experiment, there are a large number of images that must be analysed to determine the contact area of each lens throughout the loading/unloading cycle. Images of the lens array during the loading/unloading cycle are captured at intervals of 2 frames per second. Depending on the test velocity and displacement, the number of images captured can range from 100 to over 500. At $2.5\times$ and $5\times$, the field of view is $(3.4 \times 2.9)\text{ mm}^2$ and $(1.7 \times 1.4)\text{ mm}^2$, respectively. For the 1600 lens array, the $2.5\times$ objective is able to view 143 lenses and the $5\times$ objective is able to view 40 lenses. At the end of an experiment, we are required to measure thousands of individual contact areas from the collection of images. If more than one field of view is analysed during an experiment, the number of contact areas will double or triple the estimates given above. The same challenges hold for the array of 324 lenses. Therefore, an automated approach to contact area measurement and data analysis is required to analyse each adhesion experiment [16].

We chose the Matlab (Mathsoft) Image Analysis software package to automatically analyse all the separate images collected during adhesion tests and measure the contact areas

of individual lenses within each image. The following is a detailed description of the image processing steps used to measure contact areas. Image analysis occurs in two distinct steps: (1) a background image is used to determine the position of each lens within the image and (2) the experimental images are analysed to determine contact areas.

A background image of the lenses out of contact is used to determine the position of each lens within the array. The background image is blurred using a Gaussian filter. Light is not uniformly reflected back into the microscope objective through the lens arrays and blurring the image smoothes non-uniformities in illumination. The blurred image is subtracted from the background image to remove dust asperities and produce an image of uniform background intensity. Next, a threshold routine is applied to the subtracted image to create a new image with pixel intensities that are equal to zero above the threshold value and one below it. This produces a binary image where the outer edge of each lens is visible as a ring with a diameter the size of the diameter of each lens. The area within each edge is filled to produce an image that has solid circles of intensity, one for each lens, and a background of intensity zero outside each circle. Each circle is assigned a number and the centroid coordinates determined for use in the evaluation of experimental images, see figure 3(a).

For experimental images, the unprocessed background image (lenses out of contact) is subtracted from each image to remove the bases of the lenses that do not contact the substrate. A threshold is applied to the subtracted image to create a binary image with pixel intensities that are equal to zero above the threshold value and one below it. This binary image is further dilated and eroded to highlight the contact areas, if they exist, at each lens position. Each contact area in this binary image is assigned a number and the centroid, contact area, eccentricity are calculated. Finally, the centroid positions determined from the image of the lenses out of contact are used to match the centroid positions of the experimental contact areas to track the contact behaviour of each lens within the array. This method of analysis allows one to measure contact radii with a standard deviation of $\pm 7.00\ \mu\text{m}$ at $2.5\times$ and $\pm 4.30\ \mu\text{m}$ at $5\times$, which is comparable to the standard deviation of manual measurements of the same contact radii that are $\pm 9.79\ \mu\text{m}$ and $\pm 4.59\ \mu\text{m}$ for $2.5\times$ and $5\times$, respectively. This comparison was completed using both automated and manual techniques to measure the contact area of 10 lenses over 30 images having a fixed contact area. The manual measurements were conducted by manually placing a circle over the contact area and using Image Pro software to calculate the area of the circle.

The automated image analysis lends itself to additional analysis tools such as 'contact maps', described further. After each experimental image is analysed and the relevant experimental data are recorded, the intensity of the pixels within each contact area is increased by an arbitrary intensity value of 1. As the software cycles through the subsequent images, the intensity of the pixels associated with a given lens contact area increases. A temporal contact map is created for each lens in this manner. These maps are helpful because they visually represent which lenses have been in contact with the substrate the longest during the experiment. Figure 3(b) is a contact map at different portions of the loading/unloading

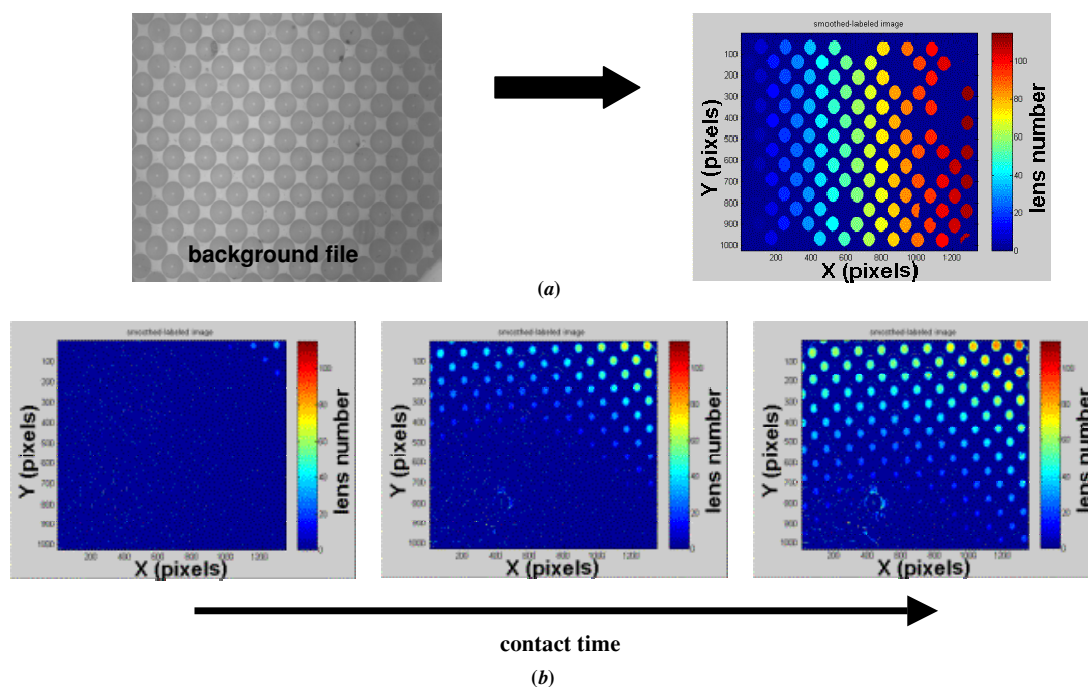


Figure 3. Image processing flow chart. (a) A background image of the lens, array not in contact with the substrate, is used to determine lens positions. These lens positions are used to determine where the lenses will be in contact during the experiment. (b) The experimental contact areas are analysed using a series of image analysis tools and a contact time map is created throughout the loading/unloading cycle.

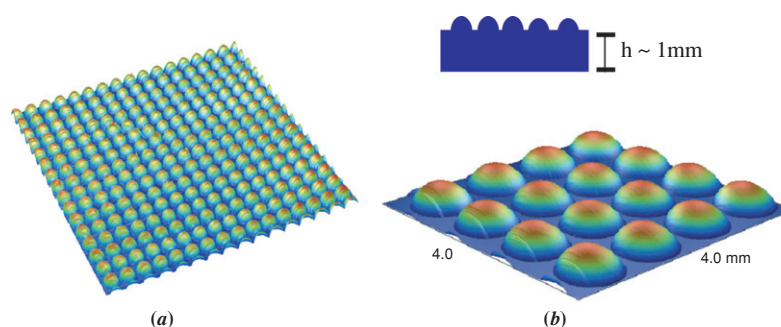


Figure 4. Profilometer images of the multilens arrays: (a) image of a portion of the smaller lens array containing 1600 lenses over 1 cm^2 ; (b) image of a portion of the larger lens array containing 324 lenses over 3.25 cm^2 . Both images are $4 \text{ mm} \times 4 \text{ mm}$ slices of their respective lens arrays. The inset drawing shows the base PDMS film that supports the lenses.

cycle for a lens array captured at $2.5\times$. The transition in colour from light blue to dark red is indicative of longer contact times between the lens and substrate. Lenses that experience similar contact deformations against the substrate can clearly be illuminated utilizing these maps. This is important for determining whether lens deformation or contact time is influential in determining the work of adhesion. While contact maps provide useful information about the experimental test, more quantitative analysis is required to extract the work of adhesion.

4. Experimental details

For these experiments, negative lens arrays are replicated in Sylgard 184 (Dow Corning) polydimethylsiloxane (PDMS) from glass or epoxy master arrays using conventional casting techniques. A second batch of PDMS is used in a ratio of 10:1 prepolymer to catalyst to form a positive lens array from the

negative mould. The PDMS is allowed to degas for several hours under vacuum and then cured at 70°C in a convection oven for 1 h. The sol fraction (uncrosslinked polymer) within the lenses is not extracted and the tensile modulus of the cured elastomer is $1.79 \text{ MPa} \pm 0.076 \text{ MPa}$. Figure 4 is a profilometer image (Dektak 8, Veeco Instruments) of both lens arrays to provide a size comparison between lenses.

The replication process results in a 1 mm thick backing of PDMS capped with the lens array (see inset to figure 4(b)). Dereuelle *et al* have shown that the placement of a thick film behind a single lens eliminates confinement effects of the lens mounting substrate and we follow this design. In their experiments, the lens radius of curvature determined from adhesion measurements using a single, small elastomeric lens ($h = 585 \mu\text{m}$ and $R = 1.17 \text{ mm}$) deviated from the true value when the thickness of the backing film was less than the height of the lens or less than $h/R \sim 0.423$, where h is the height of the lens and R is its radius of curvature.

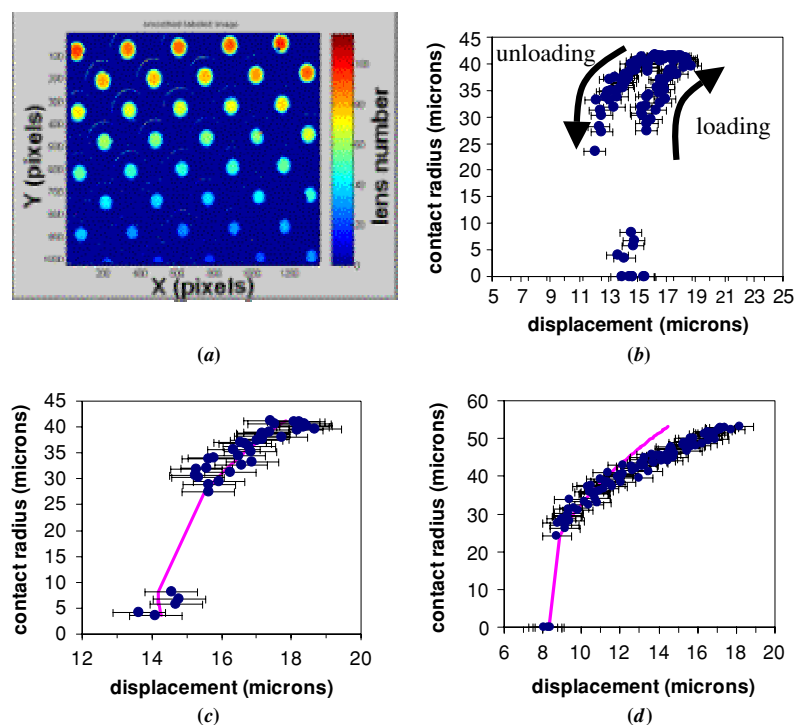


Figure 5. (a) Contact time map of lenses across the lens array at $5\times$. The shift in colour from blue to red indicates a longer contact time. (b) Experimental contact areas are analysed using a series of image analysis tools and a contact time map is created throughout the loading/unloading cycle. (c) Contact area versus displacement for the loading behaviour of one lens in the lower left corner of the lens array (a). (d) Contact area versus displacement for the loading behaviour of one lens in the upper right corner of the lens array (a). The solid line in (c) and (d) is the curve fit to the JKR theory, while the error bars represent the standard uncertainty ($\pm 0.75 \mu\text{m}$) from the displacement sensor.

For these experiments, $50 \text{ mm} \times 75 \text{ mm}$ borosilicate glass slides (Corning Glass Works) were cleaned with an excess of toluene, acetone and ethanol (all from Aldrich). After drying with nitrogen gas, the slides were cleaned in a UVO chamber for 20 min and the solvent rinse was repeated. Finally, the slides were dried using nitrogen gas. The lens array and actuator were placed $\approx 5 \mu\text{m}$ over the glass slide and the tip/tilt stage adjusted to bring the two surfaces into parallel. The lens and substrate are determined to be ‘parallel’ when a displacement of $10 \mu\text{m}$ or less brings all of the lenses within the field of view into contact and this criterion is the main reason for the large lens displacements. Adhesion tests were run at a velocity of 200 nm s^{-1} for a displacement of $15 \mu\text{m}$ with no dwell time.

5. Results and discussion

5.1. Role of lens deformation

Multilens adhesion tests were conducted at microscope magnifications of $2.5\times$ and $5\times$. Initially, we discuss use of the $5\times$ objective to determine whether the deformation of the lenses during testing affects the ability to fit the experimental data to equation (8).

An important condition of the JKR model is that the elastic hemisphere is not significantly deformed from its original shape during the contact test. The height of the lenses in this array is $\approx 22 \mu\text{m}$, which is nearly equal to the $15 \mu\text{m}$ displacement employed during the test sequence. Therefore, those lenses that contact the substrate first may be compressed

68% of their undeformed height at the maximum displacement. Gross distortion of the lenses from their original shape will lead to finite size effects that are not accounted for in the JKR theory [22, 25].

Figures 5(a) and (b) are the contact time map at $5\times$ magnification along with the contact radius–displacement curve for a single lens in the array, respectively. The transition in colour from light blue (lower left corner) to dark red (upper right corner) across the lens array in figure 5(a) is indicative of a difference in the displacement and, consequently, the deformation of the lenses between these two regions. We can compare several lenses from different regions to gain an understanding of whether lens deformations cause deviations from the JKR theory. Figures 5(c) and (d) are the experimental and fitted contact area versus displacement curves for the loading of a single lens of the multilens array within the upper right and lower left corners of the lens array, respectively. From these graphs it is apparent that the lenses that contact the glass substrate first (upper right corner) deviate from the JKR theory at the highest deformations. For this test, approximately 50% of the lenses deviate from the JKR theory in the same manner. The reason for this deviation from the JKR theory is not immediately clear, but it does not appear to correlate with indications of confinement such as the ratio of contact radius to displacement or lens height and may, ultimately, be linked to coupling between the lenses through the thick base PDMS layer. With this information, we know that the work of adhesion measured from these lenses is not indicative of the true work of adhesion. In fact, we can make use of this information to remove those

lenses that exhibit a specific ‘colour’ from future analysis. This provides a unique ability of the multilens array to not only provide high-throughput adhesion measurements, but also supply visual cues as to whether confinement effects are influencing adhesion measurements.

For those lenses whose contact behaviour can be modelled using the JKR theory, the average work of adhesion determined by fitting equation (8) to the loading curve is $(18.9 \pm 9.4) \text{ mJ m}^{-2}$ at $5\times$ and $(18.6 \pm 7.6) \text{ mJ m}^{-2}$ at $2.5\times$. The error is the standard error of the mean. These values are close to each other and both are similar to the work of adhesion $(20 \text{ mJ m}^{-2} \pm 5 \text{ mJ m}^{-2})$ measured from single-lens PDMS–glass adhesion tests³, but the error within the multilens measurements is large.

The large standard error in the determination of \mathcal{G} is believed to result from the $1.5 \mu\text{m}$ uncertainty in the displacement sensor reading. \mathcal{G} was determined from a nonlinear least-square fit of the lens data to equation (8) using the Levenberg–Marquardt algorithm. A wide range of \mathcal{G} and δ_0 values were valid to minimize the chi-square value using the standard deviations of the displacement sensor. It was difficult to dismiss one fit as better compared to another. The source of uncertainty in the displacement is related to the mounting of the displacement sensor within the MCAT and the collection of displacement voltages using the LabView software. Ultimately, this is a critical challenge for this technique as the displacement-based approach to measuring the work of adhesion relies on an accurate displacement measurement. As of publication, steps have been taken to improve LabView efficiency and the sensor mounting system to increase instrument resolution and reduce instrument error.

For those lenses whose contact behaviour deviates from the JKR theory at large displacements, the average work of adhesion determined from fitting equation (8) is $(25.1 \pm 7.5) \text{ mJ m}^{-2}$ at $5\times$ and $(25.1 \pm 8.6) \text{ mJ m}^{-2}$ at $2.5\times$.⁴ The error reported is the standard error of the mean.

5.2. Analysing unloading curves

Figure 5(b) is an example of adhesion hysteresis that occurs during adhesion tests. Adhesion hysteresis is the difference between the loading and unloading curves and is attributed to interfacial processes such as entanglement of chains across the interface [26–30], surface reorganization [31–34] and acid–base interactions [35]. These processes increase the energy required to separate the surfaces and can indicate increased adhesion at the interface. The thermodynamic work of adhesion serves as the lower bound for adhesion energy during the unloading. The adhesion energy measured during unloading is valuable because it is essential for observing these debonding processes. When significant adhesion hysteresis exists, it may not be possible to describe the unloading curve using a single work of adhesion value determined from a fit of

³ Single-lens experiments conducted on 2 mm thick PDMS films created from the same batch of PDMS as the multilens arrays. The experiments were conducted at a velocity of 200 nm s^{-1} with a glass indenter that has a radius of curvature of 1.5 mm.

⁴ The data points (large displacements) that deviated from the JKR theory were removed from the fit. Equation (8) was fitted to the data that did not deviate from JKR behaviour (small displacements). The work of adhesion reported here is from the fit to the small displacements on the a versus δ curve.

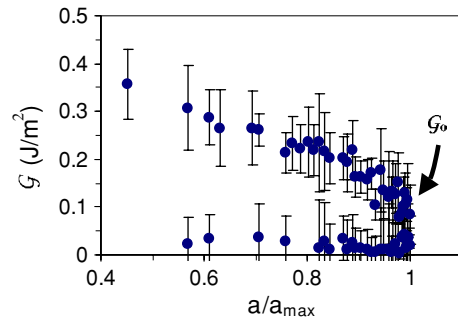


Figure 6. Energy release rate as a function of contact radius for the PDMS lens array against a glass substrate. The error represents one standard deviation in \mathcal{G} at a/a_{max} . The contact area is normalized by the maximum contact area in order to compare lenses from different positions and experiments. The $\mathcal{G}_{\text{loading}}$ curve is flat and less than $\mathcal{G}_{\text{unloading}}$ indicating adhesion hysteresis between the lenses and the glass slide. \mathcal{G}_0 has been highlighted to illustrate the energy required to first change contact area upon unloading.

equation (8) to unloading data. In this case, one must discuss the debonding process in terms of the energy release rate.

The energy release rate is given in equation (7). As stated previously, the energy release rate is the energy required to decrease the contact area a unit amount. Figure 6 is a graph of the energy release rate as a function of normalized contact radius (a/a_{max}) for the loading and unloading cycle. The contact radius has been normalized to facilitate the comparison between lenses with different contact times. The figure shows that the energy release rate for different lenses at different magnifications against the glass substrate is comparable and the unloading behaviour differs from the loading behaviour. The error bars shown in the graph are large and are attributed to the uncertainty in the displacement measurement.

Adhesion between the glass and PDMS requires a threshold amount of energy to start movement of the crack and change the contact area. This energy is given as \mathcal{G}_0 and is the energy required to first cause the contact area to change. As the lens is retracted, mechanical energy is input into the system until \mathcal{G}_0 is reached. \mathcal{G}_0 was calculated to be $(125 \pm 24.6) \text{ mJ m}^{-2}$ for $5\times$ and $(101 \pm 20.1) \text{ mJ m}^{-2}$ for $2.5\times$. These values are much larger than the work of adhesion determined from the loading curves and are an example of hysteresis occurring during contact. It should be noted that comparable single-lens tests utilizing unextracted PDMS films do not show significant adhesion hysteresis against clean glass lenses. Viscoelastic effects have been shown to increase adhesion hysteresis for soft systems. The slow indentation rate of 200 nm s^{-1} (overall strain rate of 0.002 s^{-1}) and processing of the lenses (no extraction) were chosen to minimize rate effects on the contact behaviour between the lens arrays and substrates, but a thorough investigation at several different indentation rates was not conducted to fully determine the effect of rate on lens behaviour. Another source of hysteresis is coordination between the lenses. Similar to the lenses under the highest compression retarding the deformation of neighbouring lenses at the initial stages of contact, highly compressed lenses can induce a non-equilibrium contact area for adjacent lenses during retraction. At this time, the source of adhesion hysteresis for the multilens arrays is not completely

understood and we are currently investigating the influence of lens size and mechanical properties on contact behaviour.

6. Conclusion

We have described a methodology to perform high-throughput axisymmetric contact adhesion measurements for elastic systems. The multilens arrays must be analysed differently compared to traditional JKR tests due to the inability to accurately measure load on each lens. The displacement-based JKR equation (equation (8)) was utilized to measure the work of adhesion during advancing and receding contact radius with δ_0 and \mathcal{G} as fitting parameters. The work of adhesion measured from the multilens tests was shown to agree with single-lens PDMS–glass measurements and between different multilens tests. The energy release rate (equation (7)) was shown to agree for different lenses within a single array and between different tests, although adhesion hysteresis is present in the multilens test that is not present in the single-lens test.

Microscope magnification was shown to limit the number of lenses in view during an experiment, but did not affect, within the errors of measurement, the measured work of adhesion. The use of the multilens technique has been shown to measure reasonable values of adhesion energies, but there are still several challenges. The single largest difficulty in conducting multilens adhesion tests is accurately measuring lens displacement. The uncertainty in lens displacement leads to a large uncertainty in the measured adhesion energy. Another important challenge lies in aligning the lens arrays parallel to the substrate to minimize the overall lens array displacement required to measure the work of adhesion. A reduction in the compression of the lenses across the array would minimize the influence of confinement effects. Coordination and rate effects are also potential challenges for the development of the MCAT methodology into a measurement technique. We intend to address these challenges in future publications.

Acknowledgments

This work was conducted at the NIST Combinatorial Methods Center. AMF acknowledges Dr Peter Drzal and Dr Arnaud Chiche (NIST) for helpful discussions. AMF acknowledges Dr Roman Koetitz (Rhodia, Inc.) for image analysis assistance. AMF and CMS acknowledge the National Research Council Postdoctoral Fellowship program for financial support.

Disclaimer

Certain commercial materials and equipment are identified for adequate definition of the experimental procedures. In no instance does such identification imply recommendation or endorsement by NIST that the material or equipment is necessarily the best available for the purpose.

References

- [1] Potyrailo R A, Chisholm B J, Olson D R, Brennan M J and Molaison C A 2002 Development of combinatorial chemistry methods for coatings: high-throughput screening of abrasion resistance of coatings libraries *Anal. Chem.* **74** 5105–11
- [2] Cawse J N 2001 Experimental strategies for combinatorial and high-throughput materials development *Acc. Chem. Res.* **34** 213–21
- [3] Bach H, Gambino C A, Gindin L K, Konitnsey R M, Lunney P D and Spittler K G 2003 High throughput screening methodologies for coating formulations *Polymer Preprints: Abstracts of the American Chemical Society—POLY Part 2* vol 225 (Washington, DC: American Chemical Society) p 401
- [4] Wicks D A and Bach H 2002 The coming revolution for coatings science: high throughput screening for formulations *29th Water-Borne & Higher-Solids and Powder Coatings Symp.* pp 1–24
- [5] Chattopadhyay S and Meredith J C 2003 Combinatorial studies of polymeric conducting–insulating thin film bilayer dewetting *Abstracts of Papers of the American Chemical Society* vol 226 (Washington, DC: American Chemical Society) p U367
- [6] Potyrailo R A, Chisholm B J, Morris W G, Cawse J N, Flanagan W P, Hassib L, Molaison C A, Ezbiansky K, Medford G and Reitz H 2003 Development of combinatorial chemistry methods for coatings: high-throughput adhesion evaluation and scale-up of combinatorial leads *J. Comb. Chem.* **5** 472–8
- [7] Schmatloch S, Bach H, van Benthem R A T M and Schubert U S 2004 High-throughput experimentation in organic coating and thin film research: state-of-the-art and future perspectives *Macromol. Rapid Commun.* **25** 95–107
- [8] Washburn N R, Simon C G, Tona A, Elgendy H M, Karim A and Amis E J 2002 Co-extrusion of biocompatible polymers for scaffolds with co-continuous morphology *J. Biomed. Mater. Res.* **60** 20–9
- [9] Washburn N R, Yamada K M, Simon C G, Kennedy S B and Amis E J 2004 High-throughput investigation of osteoblast response to polymer crystallinity: influence of nanometer-scale roughness on proliferation *Biomaterials* **25** 1215–24
- [10] Sormana J L and Meredith J C 2004 High-throughput discovery of structure–mechanical property relationships for segmented poly(urethane-urea)s *Macromolecules* **37** 2186–95
- [11] Stafford C M, Harrison C, Beers K L, Karim A, Amis E J, VanLandingham M R, Kim H C, Volksen W, Miller R D and Simonyi E E 2004 A buckling-based metrology for measuring the elastic moduli of polymeric thin films *Nature Mater.* **3** 545–50
- [12] Roberson S V, Fahey A J, Sehgal A and Karim A 2002 MultiFunctional ToF-SIMS: combinatorial mapping of gradient energy substrates *Appl. Surf. Sci.* **200** 150–64
- [13] Smith A P, Douglas J F, Meredith J C, Amis E J and Karim A 2001 Combinatorial study of surface pattern formation in thin block copolymer films *Phys. Rev. Lett.* **87** 015503
- [14] Smith A P, Douglas J F, Meredith J C, Amis E J and Karim A 2001 High-throughput characterization of pattern formation in symmetric diblock copolymer films *J. Polym. Sci. B* **39** 2141–58
- [15] Meredith J C, Smith A P, Karim A and Amis E J 2000 Combinatorial materials science for polymer thin-film dewetting *Macromolecules* **33** 9747–56
- [16] Meredith J C, Smith A P, Crosby A J, Amis E J and Karim A 2002 *Encyclopedia of Polymer Science and Technology* (New York: Wiley)
- [17] Meredith J C, Karim A and Amis E J 2000 High-throughput measurement of polymer blend phase behavior *Macromolecules* **33** 5760–2
- [18] Johnson K L, Kendall K and Roberts A D 1971 Surface energy and the contact of elastic solids *Proc. R. Soc. A* **324** 301

- [19] Crosby A J, Karim A and Amis E J 2003 Combinatorial investigations of interfacial failure *J. Polym. Sci. B* **41** 883–91
- [20] Crosby A J 2003 Combinatorial characterization of polymer adhesion *J. Mater. Sci.* **38** 4439–49
- [21] Mangipudi V S and Tirrell M 1998 Contact-mechanics-based studies of adhesion between polymers *Rubber Chem. Technol.* **71** 407–48
- [22] Deruelle M, Hervet H, Jandeau G and Leger L 1998 Some remarks on JKR experiments *J. Adhes. Sci. Technol.* **12** 225–47
- [23] Shull K R 2002 Contact mechanics and the adhesion of soft solids *Mater. Sci. Eng. R* **36** 1–45
- [24] Maugis D and Barquins M 1978 Fracture mechanics and the adherence of viscoelastic bodies *J. Phys. D: Appl. Phys.* **11** 1989
- [25] Ahn D and Shull K R 1996 JKR studies of acrylic elastomer adhesion to glassy polymer substrates *Macromolecules* **29** 4381–90
- [26] Koberstein J T, Duch D E, Hu W, Lenk T J, Bhatia R, Brown H R, Lingelser J P and Gallot Y 1998 Creating smart polymer surfaces with selective adhesion properties *J. Adhes.* **66** 229–49
- [27] Brown H R 1993 Effects of chain pull-out on adhesion of elastomers *Macromolecules* **26** 1666–70
- [28] Deruelle M, Leger L and Tirrell M 1995 Adhesion at the solid–elastomer interface—influence of the interfacial chains *Macromolecules* **28** 7419–28
- [29] Marciano Y, Deruelle M, Tirrell M, Hervet H and Leger L 1994 Model experiments on elastomer–solid adhesion *Vide—Sci. Tech. Appl.* 69–73
- [30] Amouroux N and Leger L 2003 Effect of dangling chains on adhesion hysteresis of silicone elastomers, probed by JKR test *Langmuir* **19** 1396–401
- [31] Silberzan P, Perutz S, Kramer E J and Chaudhury M K 1994 Study of the self-adhesion hysteresis of a siloxane elastomer using the JKR method *Langmuir* **10** 2466–70
- [32] Haidara H, Chaudhury M K and Owen M J 1995 A direct method of studying adsorption of a surfactant at solid–liquid interfaces *J. Phys. Chem.* **99** 8681–3
- [33] Chaudhury M K 1993 Surface free-energies of alkylsiloxane monolayers supported on elastomeric polydimethylsiloxanes *J. Adhes. Sci. Technol.* **7** 669–75
- [34] Girard-Reydet E, Oslanec R, Whitten P and Brown H R 2004 Effects of contact time and polarity level on adhesion between interacting surfaces *Langmuir* **20** 708–13
- [35] Choi G Y, Kang J F, Ulman A, Zurawski W and Fleischer C 1999 Acid–base interaction in the adhesion between two solid surfaces *Langmuir* **15** 8783–6
- [36] Lin Y Y, Hui C Y and Baney J M 1999 Viscoelastic contact, work of adhesion and the JKR technique *J. Phys. D: Appl. Phys.* **32** 2250–60
- [37] Lin Y Y and Hui C Y 2002 Mechanics of contact and adhesion between viscoelastic spheres: an analysis of hysteresis during loading and unloading *J. Polym. Sci. B* **40** 772–93
- [38] Giri M, Bousfield D B and Unertl W N 2000 Stress intensity in viscoelastic contacts *Tribol. Lett.* **9** 33–9
- [39] Giri M, Bousfield D B and Unertl W N 2001 Dynamic contacts on viscoelastic films: work of adhesion *Langmuir* **17** 2973–81